



**HAL**  
open science

## Estimation of Fukushima radio-caesium deposits by airborne surveys: sensitivity to the flight-line spacing

Pedram Masoudi, Mathieu Le Coz, Marc Andre Gonze, Charlotte Cazala

### ► To cite this version:

Pedram Masoudi, Mathieu Le Coz, Marc Andre Gonze, Charlotte Cazala. Estimation of Fukushima radio-caesium deposits by airborne surveys: sensitivity to the flight-line spacing. *Journal of Environmental Radioactivity*, 2020, 222, pp.106318. 10.1016/j.jenvrad.2020.106318 . hal-02929851

**HAL Id: hal-02929851**

**<https://hal.science/hal-02929851>**

Submitted on 3 Sep 2020

**HAL** is a multi-disciplinary open access archive for the deposit and dissemination of scientific research documents, whether they are published or not. The documents may come from teaching and research institutions in France or abroad, or from public or private research centers.

L'archive ouverte pluridisciplinaire **HAL**, est destinée au dépôt et à la diffusion de documents scientifiques de niveau recherche, publiés ou non, émanant des établissements d'enseignement et de recherche français ou étrangers, des laboratoires publics ou privés.



Distributed under a Creative Commons Attribution - NonCommercial - NoDerivatives 4.0 International License

1 **Estimation of Fukushima radio-caesium deposits by airborne surveys: sensitivity to the flight-line**  
2 **spacing**

3 Pedram MASOUDI<sup>1</sup>, Mathieu LE COZ<sup>1</sup>, Marc-André GONZE<sup>2</sup>, Charlotte CAZALA<sup>1</sup>

4 <sup>1</sup>Institut de Radioprotection et de Sûreté Nucléaire (IRSN), PSE-ENV/SEDRE, 31 avenue de la Division  
5 Leclerc, 92260 Fontenay-aux-Roses, France

6 <sup>2</sup>Institut de Radioprotection et de Sûreté Nucléaire (IRSN), PSE-ENV/SEREN, 13115 Saint-Paul-lez-  
7 Durance, France

8 **Highlights:**

- 9
- Geostatistical mapping of <sup>137</sup>Cs ground activity from airborne gamma-ray data
  - Punctual and characterization errors as a function of flight-line spacing
  - Sensitivity of the mapping to the spatial structure of the contamination
- 10  
11

12 **Abstract**

13 After Fukushima Daiichi Nuclear Power Plant (FDNPP) accident, airborne gamma-ray detection was  
14 used for regional mapping of soil contamination. For such surveys, the flight-line spacing is an  
15 important factor controlling the quality of contamination maps. In this study, cesium-137 (<sup>137</sup>Cs)  
16 ground activity is interpolated and mapped using ordinary kriging method; thereafter the error of  
17 interpolation is evaluated as a function of flight-line spacing. The analyses were conducted in six 20  
18 km × 20 km test sites with distance of less than 80 km from the FDNPP. In each site, the ordinary  
19 kriging estimators were applied to different selections of flight-lines of decreasing density, then  
20 punctual and classification errors were calculated. It is demonstrated that these variables are highly  
21 correlated ( $r^2 > 0.78$ ): increasing the flight-line spacing for 1 km increases the errors from 3% to 9%,  
22 depending on the site location. Therefore, flight-line spacing could be designed as a function of  
23 acceptable error, determined in the monitoring objectives.

24 **Keywords:** Geostatistical radiological mapping; flight-line spacing optimization; sampling design;  
25 nuclear accident and post-accidental monitoring.

## 26 **1. Introduction**

27 Following the major accident of the Fukushima Daiichi Nuclear Power Plant (FDNPP) in March 2011,  
28 large amounts of radionuclides were released and deposited onto the continental and oceanic  
29 surfaces (Saito and Onda, 2015). The soil gamma-ray measurements performed in July 2011 showed  
30 that more than 99% of the air dose rate originated from radio-caesium isotopes (Saito et al., 2015). In  
31 order to assess the temporal evolution of radio-caesium ground activity in contaminated territories of  
32 the Fukushima region (i.e., up to ~80 km from the FDNPP), airborne gamma-ray surveys were  
33 performed periodically since the accident (Sanada et al., 2014; Le Coz et al., 2019). The airborne  
34 sampling design varies from a survey to another; e.g., between 2011 and 2013, the spacing between  
35 flight-lines ranged from 600 m to 2 km depending on the survey (IAEA, 2014).

36 Airborne geophysical surveys are commonly used to investigate physical properties of the earth over  
37 a large region (e.g., Airo et al., 2011; Kass, 2013). The design of an airborne survey consists of  
38 determining flight-line direction and spacing, in addition to determining flight height and speed  
39 (Minty, 1997; Kass, 2013). Almost always, the acquired data is denser along the flight-lines than  
40 perpendicular to them. Hence, the flight-lines are designed parallel to the direction of maximum  
41 variability (if it exists and is known), and the flight-line spacing should be as dense as not to miss local  
42 hot-spots between lines, i.e., aliasing (Reeves, 2005). The flight-line spacing is recommended to be  
43 one kilometer or greater, for a regional or national scale inventory investigation; and between 50 m  
44 and 400 m is suggested for detailed mapping. In particular cases, e.g., individual field boundaries and  
45 search for radioactive sources, flight-line spacing could be designed to be 50 m or even less (IAEA,  
46 2003).

47 In case of nuclear accidents, where there is long-distance propagation of radionuclides through the  
48 environment, airborne gamma-ray measurement is considered to be completely relevant for post-

49 accident reconnaissance (Sanderson et al., 2001). The effect of flight-line spacing on the estimation  
50 of  $^{137}\text{Cs}$  inventory in ground was assessed in three areas of NW England and SW Scotland (Sanderson  
51 et al., 2008): the increase in flight-line spacing (subsampling), from 50 to 500 m (10 km  $\times$  10 km area)  
52 and from 500 m to 5 km (50 km  $\times$  50 km area), was shown to preserve the general outline of  
53 depositional area, and the difference in the estimated inventories was below 10%; however, local  
54 variations were not clearly defined by the sparser surveys. In fact, flight-line spacing should be  
55 designed in order to obtain an optimal trade-off between the survey costs (financial, time delay,  
56 sampling limitations, etc.) and its objectives (level of contamination, waste volume, desired  
57 resolution, etc.), which is different for every situation (Desnoyers and Dubot, 2014a, b).

58 This study aims at investigating and quantifying the effect of flight-line spacing on interpolation of  
59 the  $^{137}\text{Cs}$  ground activity from airborne gamma-ray spectrometry survey in the Fukushima region. To  
60 this end,  $^{137}\text{Cs}$  maps are generated based on subsets of measurements acquired during a relatively  
61 dense airborne survey for six 20 km  $\times$  20 km sites located within the FDNPP 80 km zone. Both  
62 punctual and classification errors are then computed from the maps obtained with various subsets.

## 63 **2. Data and method**

### 64 *2.1. Datasets*

65 After Fukushima accident, a series of gamma-ray airborne surveys were conducted by the Ministry of  
66 Education, Culture, Sports, Science and Technology (MEXT) on a semi-circle region with 80 km radius  
67 centered at the FDNPP (Fig. 1a). The counting rate at the flying altitude was converted into a deposit  
68 estimated at ground surface by applying the following transformations: (i) altitude correction to 1 m  
69 a.g.l.; (ii) conversion of count rates to dose rates; and (iii) conversion of dose rates into ground  
70 activity of  $^{137}\text{Cs}$  (in  $\text{Bq}\cdot\text{m}^{-2}$ ) (Gonze et al., 2014). The processed data and further descriptions are  
71 publicly available (JAEA, 2014).

72 The airborne measurement and the derived parameters are generally attributed to a circular area on  
73 the ground, beneath the detector, called Field of View (FOV). For the Fukushima surveys, the radius  
74 of FOV is recommended to be considered equal to the detector height, namely about 350 m (Lyons  
75 and Colton, 2012). At this height, more than 75% of recorded gamma-ray is originated from the FOV  
76 (Malins et al., 2015). In addition, since airborne measurement is performed along the flight-lines, the  
77 sampling spacing is minimum parallel to the flight-lines, about 40 m depending on the flight speed.  
78 Perpendicular to the flight-lines, the sampling spacing is significantly higher, in the order of several  
79 hundred meters, and depends on both the survey and the location (Tables 1 and 2).

80 For investigating mapping sensitivity to flight-line spacing, the 8<sup>th</sup> airborne survey (airborne #8,  
81 November 2013), which is the densest available airborne survey, was selected. The study focuses on  
82 six square 20 km × 20 km test sites (T1 to T6 on Fig. 1a and Table 2) representing a variety of  
83 geographical and land-use situations as well as a wide range of <sup>137</sup>Cs ground activity (Fig. 2). In each  
84 test site, a unique set of points (91 to 136 depending on the density of data) was kept out from the  
85 original dataset for validation purpose (Fig. 1b). Then, a series of datasets was generated by  
86 removing flight-lines (i.e., sub-sampling) in order to increase the sampling distance between flight-  
87 lines (Table 3).

## 88 *2.2. Interpolation procedure*

89 In each test site, <sup>137</sup>Cs was interpolated using each flight-line selection. The interpolation procedure,  
90 based on the geostatistical theory of kriging, was carried out by means of Isatis commercial software  
91 (Bleines et al., 2004):

- 92 i. Since the distribution of <sup>137</sup>Cs is often lognormal, it was transformed to logarithmic scale.
- 93 ii. Geostatistical methods are basically developed for interpolating stationary data (Chiles and  
94 Delfiner, 2012); previous analyses of Fukushima airborne data yet showed that variability in  
95  $\log(^{137}\text{Cs})$  is generally nonstationary in distance of 20 km (Masoudi et al., 2019). Since

- 96 experimental semi-variogram is not conformable, a trend (deterministic model) was thus  
97 fitted by moving average (Table 4) and removed from  $\log(^{137}\text{Cs})$ , resulting in residual.
- 98 iii. The distribution of residual was transformed to the normal Gaussian distribution through the  
99 frequency inversion anamorphosis algorithm (Bleines et al., 2004).
- 100 iv. The experimental semi-variogram of residual was computed and a spherical model was  
101 fitted. For various distances between pairs of points, the semi-variogram describes the half  
102 mean of square difference in residual (Chiles and Delfiner, 2012).
- 103 v. Point ordinary kriging was applied to estimate the residual at the location of validation points  
104 (Fig. 1b). This kriging system considers that mean of data around the estimation point is  
105 constant but unknown (Wackernagel, 2003).
- 106 vi. The punctual estimations were back transformed to the pre-anamorphosis distribution,  
107 summed with the deterministic model and back transformed to the scale of initial data, in  
108 order to be comparable with  $^{137}\text{Cs}$  values at validation points.
- 109 vii. Ordinary block kriging was applied to estimate the average residual on square grid cells with  
110 250 m sides covering whole the area of test site. Indeed, the block kriging system is an  
111 adaptation of point kriging for continuous data within surface or volume (Wackernagel,  
112 2003).
- 113 viii. The estimated values were back transformed to the pre-anamorphosis distribution, summed  
114 with the deterministic model and back transformed to the scale of initial data, in order to  
115 produce  $^{137}\text{Cs}$  contamination map.

116 The kriging interpolation procedure not only provides an estimated value but also variance of  
117 estimation error, a measure of estimation uncertainty (Journel et al., 2000). Kriging estimations and  
118 variances were used in turning bands simulation in order to generate 100 possible realizations of  
119 the  $^{137}\text{Cs}$  map (Chiles and Delfiner, 2012). The simulation was done for each flight-line selection on  
120 test site T1.

121 2.3. Interpolation errors

122 The punctual error was computed by comparing  $^{137}\text{Cs}$  values estimated at the validation points  
123 through point ordinary kriging by considering each flight-line selection and all flight lines:

$$124 E_p = \frac{1}{n} \sum_{i=1}^n \frac{|v_i^{sel} - v_i^{all}|}{v_i^{all}} \quad [\text{Eq. 1}]$$

125 were  $E_p$  is the punctual error;  $n$  is the number of validation points;  $v_i^{sel}$  and  $v_i^{all}$  are estimated  $^{137}\text{Cs}$   
126 ground activity ( $\text{kBq.m}^{-2}$ ) at point  $i$  using a selection of flight-lines and all flight-lines, respectively.

127 The  $^{137}\text{Cs}$  contamination maps produced by ordinary block kriging interpolation were used to classify  
128 each test site to contaminated and not contaminated areas, given a contamination threshold.  
129 Overlapping real and estimated contamination areas partitions each test site to four surfaces (Fig. 3),  
130 and a classification error is computed as the ratio of misclassified surfaces to the real contamination  
131 area:

$$132 E_c = \frac{S2+S3}{S1+S2} \quad [\text{Eq. 2}]$$

133 where  $E_c$  is the classification error;  $S1$  is correctly characterized contaminated surface;  $S2$  and  $S3$  are  
134 false negative and false positive characterized surfaces, respectively. In practice, the real  
135 contaminated area is unknown, however the contamination map, produced using all the flight-lines,  
136 resembles to the reality the most. Hence, this map is considered as the reference for calculating the  
137 classification error of other flight-line selections. This error is calculated as a function of  
138 contamination threshold.

139 In the interpolation procedure (Sect.2.2), the flight-line spacing influences the variography analysis  
140 (stage iv) and controls the neighboring data configuration of kriging estimators (stages v and vii). In  
141 order to measure the sensitivity of results to variogram model, interpolation procedure was repeated  
142 in test site T1 for all the selections, using the fixed variogram computed using all flight-lines. Both the

143 punctual and classification errors were then computed and compared to the errors computed by  
144 updated models.

#### 145 2.4. Kriging uncertainty

146 In test site T1, the influence of increasing flight-line spacing on the kriging uncertainty was  
147 investigated based on the sets of 100 realizations generated by turning bands simulation. More  
148 precisely, the relation between the flight-line spacing and the average of standard deviations of the  
149 simulated  $^{137}\text{Cs}$  values (i.e., on the 100 realizations) at each validation point were analyzed. In  
150 addition, the relation between the flight-line spacing and standard deviation of the misclassified area  
151 computed based on the 100 realizations for a given threshold was analyzed.

### 152 3. Results

#### 153 3.1. *Experimental semi-variograms*

154 The experimental semi-variograms computed orthogonal to the flight-lines (Fig. 4) shows that spatial  
155 correlation of  $^{137}\text{Cs}$  is the shortest for test site T2, lower than 5 km. In this test site, the increase of  
156 flight-line spacing clearly impacts the quality of the experimental semi-variogram: in 1/3 sub-  
157 sampling, the flight-line spacing becomes larger than spatial correlation (Fig. 4b). The experimental  
158 semi-variograms computed for test site T4 also show a relatively short spatial correlation, about 5  
159 km, which cannot be identified from the scarcer sub-sampling (Fig. 4d). For the other test sites, the  
160 experimental semi-variograms show similar behavior whatever the sub-sampling, particularly for the  
161 test site T3, for which the spatial correlation is the longest, farther than 15 km (Fig. 4c).

#### 162 3.2. *Punctual and classification errors*

163 In test site T1, the cross-plot of punctual error versus flight-line spacing shows a high positive  
164 correlation ( $r^2=0.86$ , Fig. 5). This relationship was modeled by fitting a linear regression, revealing  
165 that increase of one kilometer in flight-line spacing results in 4% increase in the punctual error, with

166 an uncertainty range of less than  $\pm 1\%$  for shortest flight-line spacing up to  $\pm 5\%$  for 5 km flight-line  
167 spacing. The punctual errors computed in test sites T2 to T5 are compatible with the linear regression  
168 model established for T1. However, the punctual error increases more rapidly in T6, i.e., 8% increase  
169 in error for 1 km increase in flight-line spacing (Fig. 5).

170 In test site T1, increasing the flight-line spacing from 1.3 to 4.0 km increases the classification error  
171 two to three times whatever the threshold value (the classification error is yet more marked for high  
172 threshold values, i.e., a small contaminated areas) (Fig. 6). Particularly, at threshold P75, i.e. the third  
173 quartile (Table 2), of the same test site, there is a strong linear correlation ( $r^2=0.79$ ) between the  
174 classification error and flight-line spacing (Fig. 6). This relationship was fitted by a linear regression  
175 model showing that the increase of one kilometer in the flight-line spacing increases the classification  
176 error by 5%. The dispersion pattern of the points around the regression line shows lower uncertainty  
177 ( $\pm 5\%$ ) in small flight-line spacing than in large flight-line spacing ( $\pm 10\%$ ) (Fig. 7). The classification  
178 error values computed in test sites T4, T5 and T6 are compatible with the linear regression model  
179 established in T1; but estimations in T2 and T3 tend to maximize and minimize the classification  
180 error, respectively.

181 For test site T1, using a fixed variogram model results in nearly the same punctual errors as updated  
182 variogram (Fig. 8a), illustrating that the punctual error is not significantly sensitive to the accuracy of  
183 variogram model. By contrast, the fixed variogram model results in significantly lower classification  
184 errors (maximum 21%) than updated variogram model, especially for the high error values (Fig. 8b),  
185 illustrating that the classification error is very much sensitive to the variography model.

### 186 3.3. Kriging uncertainty

187 For test site T1, the average of standard deviations of  $^{137}\text{Cs}$  values simulated at the validation points  
188 increases proportional to flight-line spacing. Using all flight-lines (0.9 km flight-line spacing), standard  
189 deviation of simulated values is about 12% of the estimation, and using one line out of five (2.5 km  
190 flight-line spacing), standard deviation of simulated values reaches 40% of estimation (Fig. 9). For a

191 contamination threshold of  $732 \text{ kBq.m}^{-2}$  (P75 of test site T1), the standard deviation of the  
192 misclassified area computed based on simulation corresponds to 7% of the estimated misclassified  
193 area using all flight-lines and 17% of the estimated value when one line out of five are considered  
194 (Fig. 9).

#### 195 **4. Discussion**

196 The analysis of punctual error shows that, in general, adding one kilometer to the flight-line spacing  
197 results in 4% increase in the mean difference between measured and estimated  $^{137}\text{Cs}$  ground activity  
198 at a given point. This increase in punctual error appears to be mainly controlled by the neighboring  
199 data configuration of kriging estimators and less sensitive to the variogram model. The relationship  
200 between punctual error and flight-line spacing can thus expected to be robust, as supported by  
201 similar results obtained in test sites T1 to T5. However, the increase in punctual error is significantly  
202 more marked for test site T6. A deeper analysis of the airborne #8 data set over the whole area of  
203 interest highlighted that the statistical distribution of  $^{137}\text{Cs}$  shows a peak at  $6885 \text{ Bq.m}^{-2}$ . This could  
204 be assimilated to a detection limit. In the test site T6, 17% of the data are set to this value, while less  
205 than 2% of the data in the other test sites (Table 2). Uneven presence of fixed values at detection  
206 limit ( $6885 \text{ Bq.m}^{-2}$ ), decreases predictability of ground activity, which explains high punctual error of  
207 T6 (Figure 5).

208 The analysis of classification error shows that adding one kilometer to the flight-line spacing results  
209 in 5% mean increase in the proportion of misclassified contaminated areas (false positive or false  
210 negative). This increase in classification error is clearly influenced from the variogram model, thus  
211 could be strongly linked to the spatial structure of the  $^{137}\text{Cs}$  ground activity: in particular, when  
212 distance of spatial correlation (i.e., variogram range) of the ground activity is short, its identification  
213 requires a dense flight-line pattern, whereas for contamination with farther distance of spatial  
214 correlation flight-line density might be less dense. The experimental semi-variograms computed  
215 orthogonal to the flight-lines shows that distance of spatial correlation of activity is the minimum for

216 test site T2 and the maximum for test site, which thus explains the most (T2) and the least (T3)  
217 classification errors. Overall, by increasing flight-line spacing, complexities and detailed variations of  
218 contamination structure disappear, and the geometric anisotropy, i.e., directivity, of contamination  
219 seems to lose its original form (Fig. 10), especially when focusing on high contamination threshold  
220 (i.e., small areas with high activity values).

221 Analyzing realizations generated by turning bands simulation revealed that the kriging uncertainty  
222 also increases with the increase of flight-line spacing: adding one kilometer to the flight-line spacing  
223 increases the standard deviation of a punctual estimation by about 6%; and increases the standard  
224 deviation of the misclassified area by about 3%. The order of magnitude of the increase of kriging  
225 uncertainty is thus similar to that of punctual and classification errors.

226 Based on the regression error models established in Figs. 5 and 7, the punctual and classification  
227 errors for each test site are calculated for the other airborne campaigns (Table 5). For the entire test  
228 sites, the errors associated to the latest airborne campaign are about half of those calculated in the  
229 earliest campaign, i.e., airborne #4. Otherwise, monitoring and contamination characterization is  
230 more accurate in newer airborne campaigns which have denser flight-lines. Since the cost of input  
231 data, here flight-line spacing, should be designed according to the value of produced map (Desnoyers  
232 and Dubot 2014a, b); such error models could be used in the financial feasibility studies in order to  
233 find the optimum flight-line spacing regarding flight cost, decontamination cost and environmental  
234 cost from one side, and the goal and value of final contamination map from the other side. As an  
235 example, the same flight-line spacing results in more accurate inventory estimation than zonation of  
236 polluted soil for decontamination planning. The reason is that the false positive and false negative  
237 errors neutralize each other in inventory estimation, however each of them participate in increasing  
238 zonation error.

## 239 **5. Conclusion**

240 The advantages of geophysical airborne data, i.e., good coverage, regular data coordination, rapid  
241 acquisition and repeatability, make airborne surveys effective in contamination characterization over  
242 a large area. The quality of contamination map produced from the airborne data is yet according to  
243 flight-induced parameters such as the FOV or the flight-line spacing.

244 In this study, the relation between flight-line spacing and two characterization errors (punctual  
245 groundsurface activity and contaminated area according to  $^{137}\text{Cs}$  threshold) is quantified in six  
246 different test sites within the contaminated Fukushima region. Both the errors are positively  
247 correlated with the flight-line spacing. In general, adding one kilometer to the flight-line spacing  
248 results in: (i) 4% increase in the mean difference between measured and estimated groundsurface  
249 activity at a given point; and (ii) 5% increase in the proportion of misclassified contaminated areas  
250 (false positive or false negative). These two errors measure different aspects of contamination. The  
251 punctual error measures the error on point estimation of groundsurface activity, while the  
252 classification error measures the error on zonation for a given threshold. The former appears to be  
253 mainly sensitive to the configuration and density of neighboring data, whereas the latter is clearly  
254 influenced from the variography analysis. Therefore the accuracy of variography is less important in  
255 point groundsurface activity estimation while it is a crucial controlling factor in zonation of  
256 contaminated area. In addition, it seems the punctual estimations are more impacted from the  
257 increase of flight-line spacing, when the proportion of values below the detection limit in the initial  
258 dataset is large.

259 Practically, for punctual estimation, the accuracy of measurements is probably more crucial than  
260 flight-line spacing. On the other hand, for surface characterization, the flight-line spacing needs to be  
261 decided relative to the spatial structure of contamination. The order of magnitude of the increase of  
262 error was shown to be similar to that of the increase of uncertainty ranges related to punctual value  
263 and misclassified; it can thus be informative to compute these ranges, e.g., based on a simulation

264 approach. Then, the issue of the optimal density of flight-lines can be tackled by asking the question:  
265 does the uncertainty range is sufficient for characterizing the variable under study?

266 For overcoming limitations resulting from a scarce flight-line spacing, a relevant solution would thus  
267 consist of integrating the airborne data with other available datasets that are more precise in order  
268 to benefit from the positive aspects of multiple datasets, e.g., precision of soil data, abundance of  
269 carborne data and good regular coverage of airborne data, e.g., using Bayes' rule (Wainwright et al.  
270 2017, 2018) or co-kriging algorithm.

### 271 **Acknowledgements and disclaim**

272 The study has been conducted in the context of the TERRITORIES project, and has received funding  
273 from the Euratom research and training program 2014-2018 in the framework of the CONCERT [grant  
274 agreement No 662287]. Japan Atomic Energy Agency (JAEA) is acknowledged for providing  
275 Fukushima airborne datasets accessible for the public and permitting publication of scientific results.  
276 Finally, the authors would like to thank Bruno Cessac, Christelle Courbet, Erwan Manach and  
277 Christophe Debayle for the scientific and technical exchanges.

278 This publication reflects only the author's view. Responsibility for the information and views  
279 expressed therein lies entirely with the authors. The European Commission is not responsible for any  
280 use that may be made of the information it contains.

### 281 **References**

282 Airo, M.L., Hautaniemi, H., Ville Korhonen, J., Kurimo, M., Levaniemi, H., 2011. Airborne geophysical  
283 data management and interpretation. Special Paper - Geological Survey of Finland 49, 349-358.  
284 Bleines, C., Perseval, S., Rambert, F., Renard, D., Touffait, Y., 2004. ISATIS Software Manual,  
285 Reference Guide, 5th edn. Geovariances & Ecole des Mines de Paris.

286 Chiles, J.P., Delfiner, P., 2012. Geostatistics, modeling spatial uncertainty, 2nd edn. A John Wiley &  
287 Sons, Inc., Hoboken, New Jersey.

288 Desnoyers, Y., Dubot, D., 2014a. Importance des données pour les cartographies géostatistiques de  
289 contaminations radiologiques. *Spectra Analyse* 296, 44-48.

290 Desnoyers, Y., Dubot, D., 2014b. Characterization of radioactive contamination using geostatistics.  
291 *Nuclear Engineering International* 59, 16-18.

292 Gonze, M.A., Renaud, P., Korsakissok, I., Kato, H., Hinton, T.G., Murlon, C., Simon-Cornu, M., 2014.  
293 Assessment of dry and wet atmospheric deposits of radioactive aerosols: Application to Fukushima  
294 radiocaesium fallout. *Environ. Sci. Technol.* 48, 11268–11276. doi: 10.1021/es502590s

295 IAEA, 2003. Guidelines for radioelement mapping using gamma ray spectrometry data. IAEA-  
296 TECDOC-1363, IAEA, Vienna.

297 Japan At. Energy Agency (JAEA), 2014. Database for radioactive substance monitoring data [WWW  
298 Document]. URL <https://emdb.jaea.go.jp/emdb> (accessed 2.12.19).

299 Japan Aerosp. eXplor. Agency (JAXA), 2018. High-resolution land use and land cover map products  
300 (©JAXA) [WWW Document]. URL [https://www.eorc.jaxa.jp/ALOS/en/lulc/lulc\\_index.htm](https://www.eorc.jaxa.jp/ALOS/en/lulc/lulc_index.htm) (accessed  
301 2.12.19).

302 Journel, A., Kyriakidis, P.C., Mao, S., 2000. Correcting the Smoothing Effect of Estimators: A Spectral  
303 Postprocessor. *Math. Geol.* 32(7), 787-813. Doi: 10.1023/A:1007544406740

304 Kass, A., 2013. Consequences of flight height and line spacing on airborne (helicopter) gravity  
305 gradient resolution in the Great Sand Dunes National Park and Preserve, Colorado. *The Leading Edge*  
306 32, 932-938. doi: 10.1190/tle32080932.1

307 Le Coz, M., Masoudi, P., Cazala, C., 2019. Saptio-temporal variation in cesium-137 ground activity,  
308 two years following Fukushima nuclear accident. Manuscript submitted for publication.

309 Lyons, C., Colton, D., 2012 Aerial measuring system in Japan. *Health Phys.* 102, 509-515. doi:  
310 10.1097/HP.0b013e31824d0056

311 Malins, A., Okumura, M., Machida, M., Takemiya, H., Saito, K., 2015. Fields of view for environmental  
312 radioactivity. In: *Proceedings of the international symposium on radiological issues for Fukushima's*  
313 *revitalized future*, pp 28-34.

314 Masoudi, P., Le Coz, M., Cazala, C., Saito, K., 2019. Spatial properties of soil analyses and airborne  
315 measurements for reconnaissance of soil contamination by <sup>137</sup>Cs after Fukushima nuclear accident in  
316 2011. *J. Environ. Radioact.* 202, 74-84. doi: 10.1016/j.jenvrad.2018.11.014

317 Minty, B.R.S., 1997. *Fundamentals of airborne gamma-ray spectrometry.* AGSO Journal of Australian  
318 *Geology and Geophysics* 17, 39-50.

319 Rabus, B., Eineder, M., Roth, A., Bamler, R., 2003. The shuttle radar topography mission (SRTM) - A  
320 new class of digital elevation models acquired by spaceborne radar. *ISPRS J. Photogramm. Remote*  
321 *Sens.* 57, 241-262. doi:10.1016/S0924-2716(02)00124-7

322 Reeves, C., 2005. *Aeromagnetic Surveys: Principles, Practice and Interpretation.* Earth-works,  
323 Washington DC.

324 Saito, K., Onda, Y., 2015. Outline of the national mapping projects implemented after the Fukushima  
325 accident. *J. Environ. Radioact.* 139, 240-249. doi: 10.1016/j.jenvrad.2014.10.009

326 Sanada, Y., Sugita, T., Nishizawa, Y., Kondo, A., To, T., 2014. The aerial radiation monitoring in Japan  
327 after the Fukushima Daiichi nuclear power plant accident. *Progress in Nuclear Science and*  
328 *Technology* 4, 76-80. doi: 10.15669/pnst.4.76

329 Sanderson, D.C.W., Cresswell, A.J., White, D.C., 2008. The effect of flight line spacing on radioactivity  
330 inventory and spatial feature characteristics of airborne gamma-ray spectrometry data. *Int. J.*  
331 *Remote Sens.* 29, 31-46. doi: 10.1080/01431160701268970

332 Sanderson, D.C.W., Cresswell, A.J., White, D.C., Murphy, S., McLeod, J., 2001. Investigation of Spatial  
 333 and Temporal Aspects of Airborne Gamma Spectrometry. Project Report, Department of the  
 334 Environment, Transport and the Regions, East Kilbride.

335 Wackernagel, H., 2003. Multivariate geostatistics: an introduction with applications, 3rd edn.  
 336 Springer-Verlag Berlin Heidelberg GmbH, Heidelberg.

337 Wainwright, H.M., Seki, A., Chen, J., Saito, K., 2017. A multiscale Bayesian data integration approach  
 338 for mapping air dose rates around the Fukushima Daiichi Nuclear Power Plant. J. Environ. Radioact.  
 339 167, 62-69. doi: 10.1016/j.jenvrad.2016.11.033

340 Wainwright, H.M., Seki, A., Mikami, S., Saito, K., 2018. Characterizing regional-scale temporal  
 341 evolution of air dose rates after the Fukushima Daiichi Nuclear Power Plant accident. J. Environ.  
 342 Radioact. 189, 213-220. doi: 10.1016/j.jenvrad.2018.04.006

### 343 **Tables**

344 Table 1. Specifications of the airborne survey datasets #3 to #8 available from the MEXT in the  
 345 Fukushima region.

Airborne	#3	#4	#5	#6	#7	#8
Start date	04.06.2011	25.10.2011	22.06.2012	31.03.2012	27.08.2013	05.11.2013
End date	02.07.2011	05.11.2011	28.06.2012	15.11.2012	18.09.2013	18.11.2013
Base date	02.07.2011	05.11.2011	28.06.2012	16.11.2012	28.09.2013	19.11.2013
<sup>137</sup> Cs mean (kBq/m <sup>2</sup> )	402	193	313	230	310	280
Flight-line spacing (m)	1.8-2 km	1.8-2 km	1.8 km	1.8 km	0.6-0.9 km	0.6-0.9 km

346

347 Table 2. Specifications of each test site selected for the study.

	T1	T2	T3	T4	T5	T6
Flight-line spacing (m)	920	920	840	960	610	920
Mean survey	356	368	355	362	356	369

altitude (m agl)						
Mean distance between measurements along flight-lines (m)	51	43	46	44	51	49
Number of validation data	100	100	100	91	136	92
<sup>137</sup> Cs distribution	lognormal	semi-gaussian	lognormal	lognormal	lognormal	lognormal
<sup>137</sup> Cs mean (kBq/m <sup>2</sup> )	509	73	122	94	1424	63
<sup>137</sup> Cs 3 <sup>rd</sup> quartile (P75) (kBq/m <sup>2</sup> )	732	93	131	115	1852	42
<sup>137</sup> Cs = 6885 Bq/m <sup>2</sup> (% of the area)	0	1.9	2.2	0.2	0	17.5

348

349 Table 3. Flight-line selections and the average of the flight-line spacing for test site T1 (see Fig 1b).

350 Selection 1/j-k means one line is selected every j successive lines. k varies from 1 to j, and represents

351 all the possible selections of one line every j lines.

Name	Selected lines			Flight-line spacing (m)
	LW	L	LE	
All the lines	all	all	all	920
Selection 1/2-1	1-2-3-4-5-7-8-9-10-11	2-4-6-8-10	1-2-5-6-9-10-13-14-17-18-21	1270
Selection 1/2-2	2-3-4-5-6-9-10-11	1-5-7-9-11	3-4-7-8-11-12-15-16-19-20	1270
Selection 1/3-1	1	2-3-4-5-6-7-8-9-10-11	1	1840
Selection 1/3-2	3-4-5-6-7-8-9-10-11	1	4-6-8-10-12-14-16-18-20	2030
Selection 1/3-3	2-4-5-7-8-9-10-11	-	2-5-7-9-11-13-15-17-19-21	2030
Selection 1/4-1	1-3-7-8-11	5-9	1-4-7-12-15-20	2530
Selection 1/4-2	3-6-7-10-11	3-4-8	10-13-18-21	2530
Selection 1/4-3	2-5-8-9	3-6	2-5-8-14-17-20	2890
Selection 1/4-4	4-7-8-11	2-5-9	7-12-15-20	2890
Selection 1/5-1	1-3-5-8-10	6-11	1-5-8-15-18	2890
Selection 1/5-2	5-7-10	1-3-8	9-12-19	3380

Selection 1/5-3	2-4-7-9	5-10	2-6-13-16	3380
Selection 1/5-4	2-4-6-11	7-9	3-7-10-17-20	3380
Selection 1/5-5	6-8-11	2-4-9	11-14-21	3380
Selection 1/6-1	1	3-5-7-9-11	1	3380
Selection 1/6-2	4-6-8-10	1	6-10-14-18	4050
Selection 1/6-3	2-4-6-8-10	-	2-7-11-15-19	4050
Selection 1/6-4	2	4-6-8-10	3	4050
Selection 1/6-5	5-7-9-11	2	12-16-20	4050
Selection 1/6-6	3-5-7-9-11	-	4-9-13-17-21	4050
Selection 1/7-1	1-4-6-11	8	1-6-11-20	4050
Selection 1/7-2	4-9-11	1-6	7-16-21	4050
Selection 1/7-3	2-7-9	4-11	2-12-17	4050
Selection 1/7-4	2-5-7	9	3-8-13	5060
Selection 1/7-5	5-10	2-7	9-18	5060
Selection 1/7-6	3-8-10	5	4-14-19	5060
Selection 1/7-7	3-6-8	10	5-10-15	5060

352

353 Table 4. Specification of interpolation procedure in each test site.

		T1	T2	T3	T4	T5	T6
Data preparation	Logarithmic transformation (cf. stage i, Fig.2)	✓	✓	×	×	×	×
	Deterministic model (cf. stage ii-ii, Fig. 2)	✓ (Average 10km)	✓ (Average 5km)	×	×	×	×
Results	Zonal anisotropy (according to variography, stage iv, Fig. 2)	✓	×	✓ (Strongly)	✓	✓ (Strongly)	✓
	Geometric anisotropy	135°	45°	115°	22° (Slightly)	135°	110°

354

355 Table 5. Generalization of the errors calculated from campaign airborne #8 to airborne campaigns #3

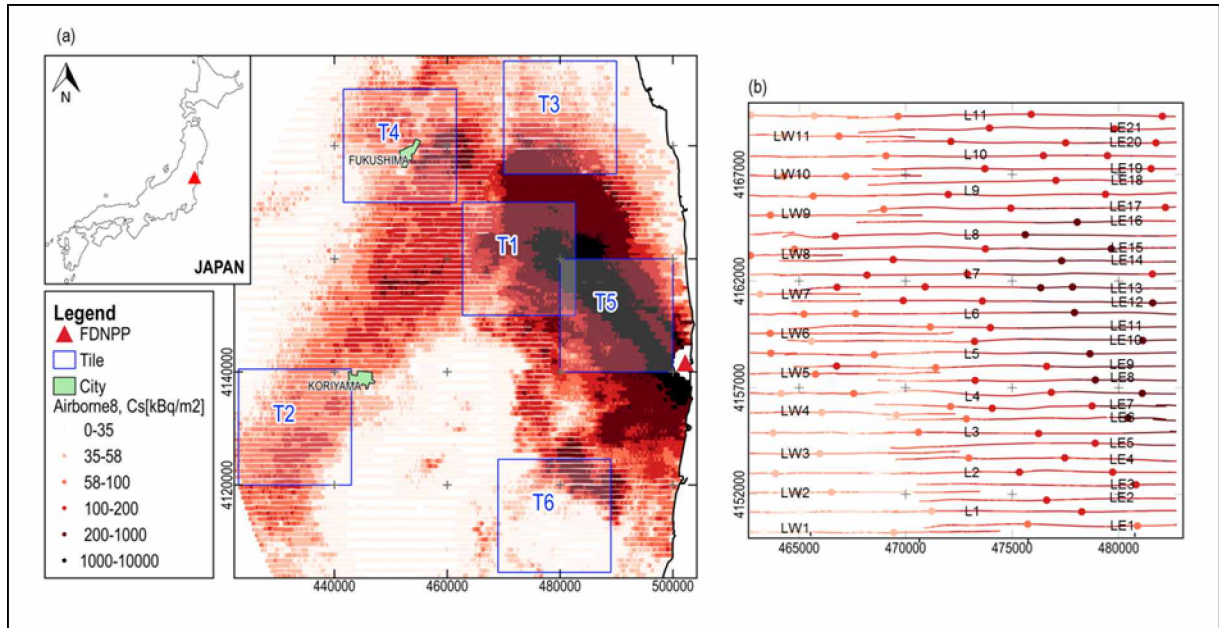
356 to #7.

Test site	Airborne	Base date	Flight-line spacing [km]	Punctual error	Classification error
T1	#3	02.07.2011	1.8	8%	10%
	#4	05.11.2011	1.8	8%	10%

	#5	28.06.2012	1.8	8%	10%
	#6	16.11.2012	1.8	8%	10%
	#7	28.09.2013	0.6	3%	4%
	#8	19.11.2013	0.6	3%	4%
T2	#3	02.07.2011	2	9%	19%
	#4	05.11.2011	2	9%	19%
	#5	28.06.2012	1.8	8%	17%
	#6	16.11.2012	1.8	8%	17%
	#7	28.09.2013	0.9	5%	9%
	#8	19.11.2013	0.9	5%	9%
T3	#3	02.07.2011	2	9%	6%
	#4	05.11.2011	2	9%	6%
	#5	28.06.2012	1.8	8%	5%
	#6	16.11.2012	1.8	8%	5%
	#7	28.09.2013	0.9	5%	3%
	#8	19.11.2013	0.9	5%	3%
T4	#3	02.07.2011	2	9%	11%
	#4	05.11.2011	2	9%	11%
	#5	28.06.2012	1.8	8%	10%
	#6	16.11.2012	1.8	8%	10%
	#7	28.09.2013	0.9	5%	6%
	#8	19.11.2013	0.9	5%	6%
T5	#3	02.07.2011	1.8	8%	10%
	#4	05.11.2011	1.8	8%	10%
	#5	28.06.2012	1.8	8%	10%
	#6	16.11.2012	1.8	8%	10%
	#7	28.09.2013	0.6	3%	4%
	#8	19.11.2013	0.6	3%	4%
T6	#3	02.07.2011	1.8	13%	10%
	#4	05.11.2011	1.8	13%	10%
	#5	28.06.2012	1.8	13%	10%
	#6	16.11.2012	1.8	13%	10%
	#7	28.09.2013	0.9	6%	6%
	#8	19.11.2013	0.9	6%	6%

357

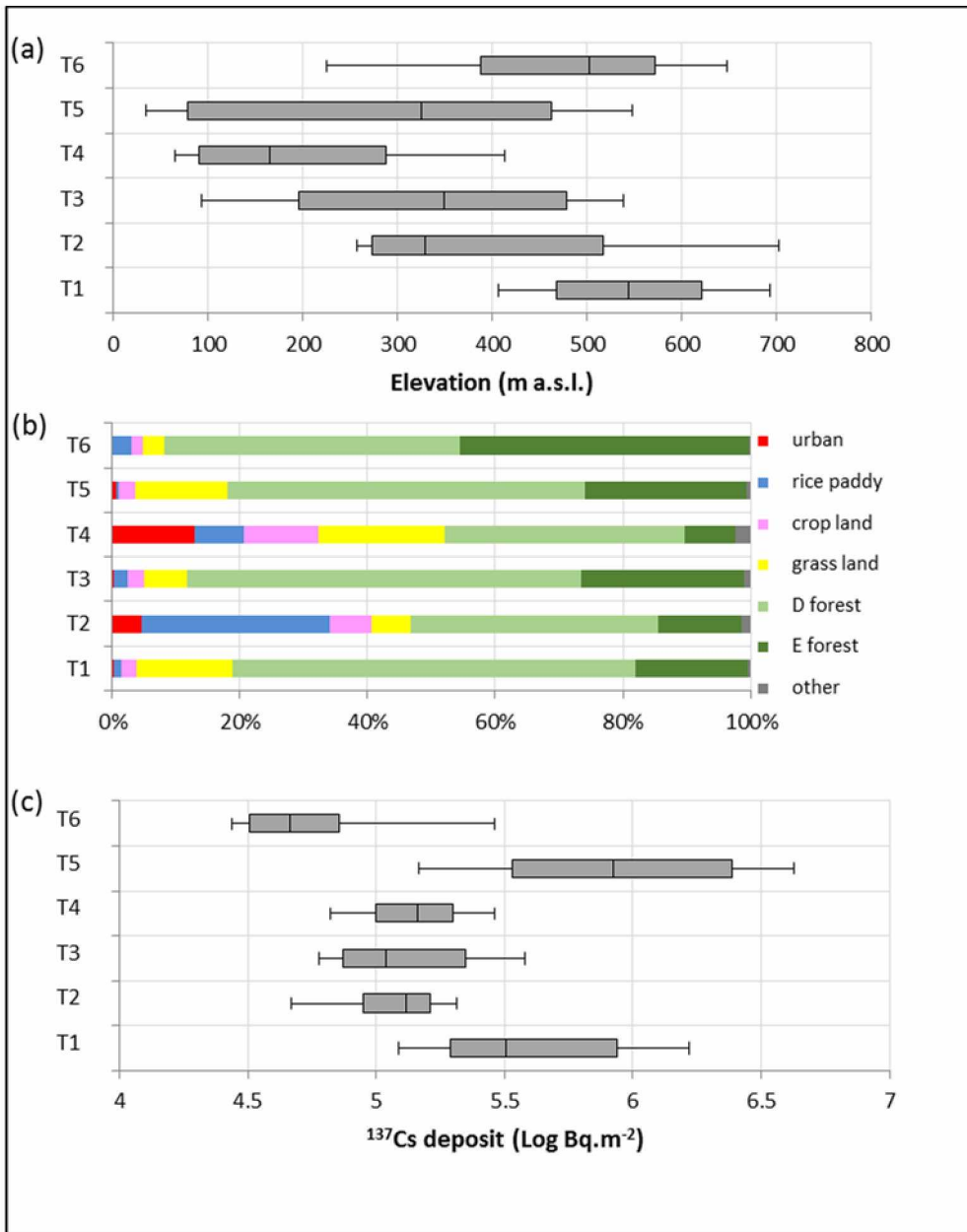
358 **Figure captions**



359

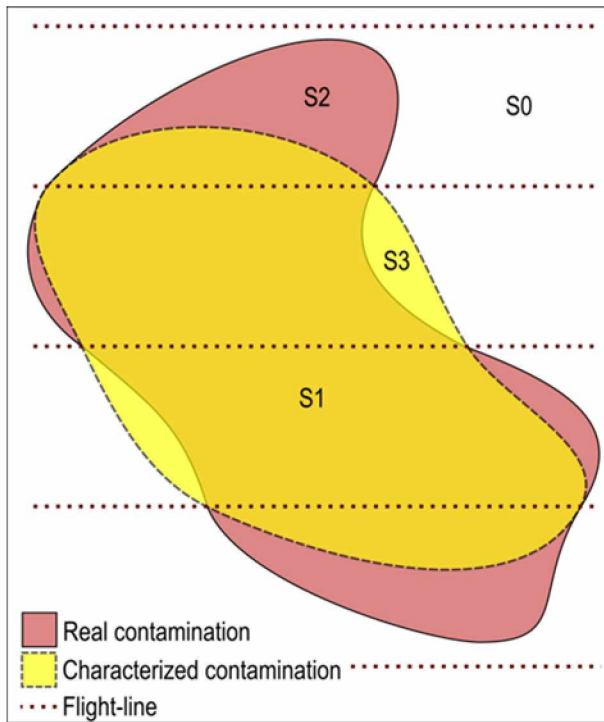
360 Fig. 1. Location of six test sites selected in this study (a). Location of flight-lines of airborne #8 inside  
 361 test site T1 (b). The validation data are bolded. L: a complete flight-line, LE (LW): an incomplete flight-  
 362 line, which extends to the Eastern (Western) border of the test site.

363



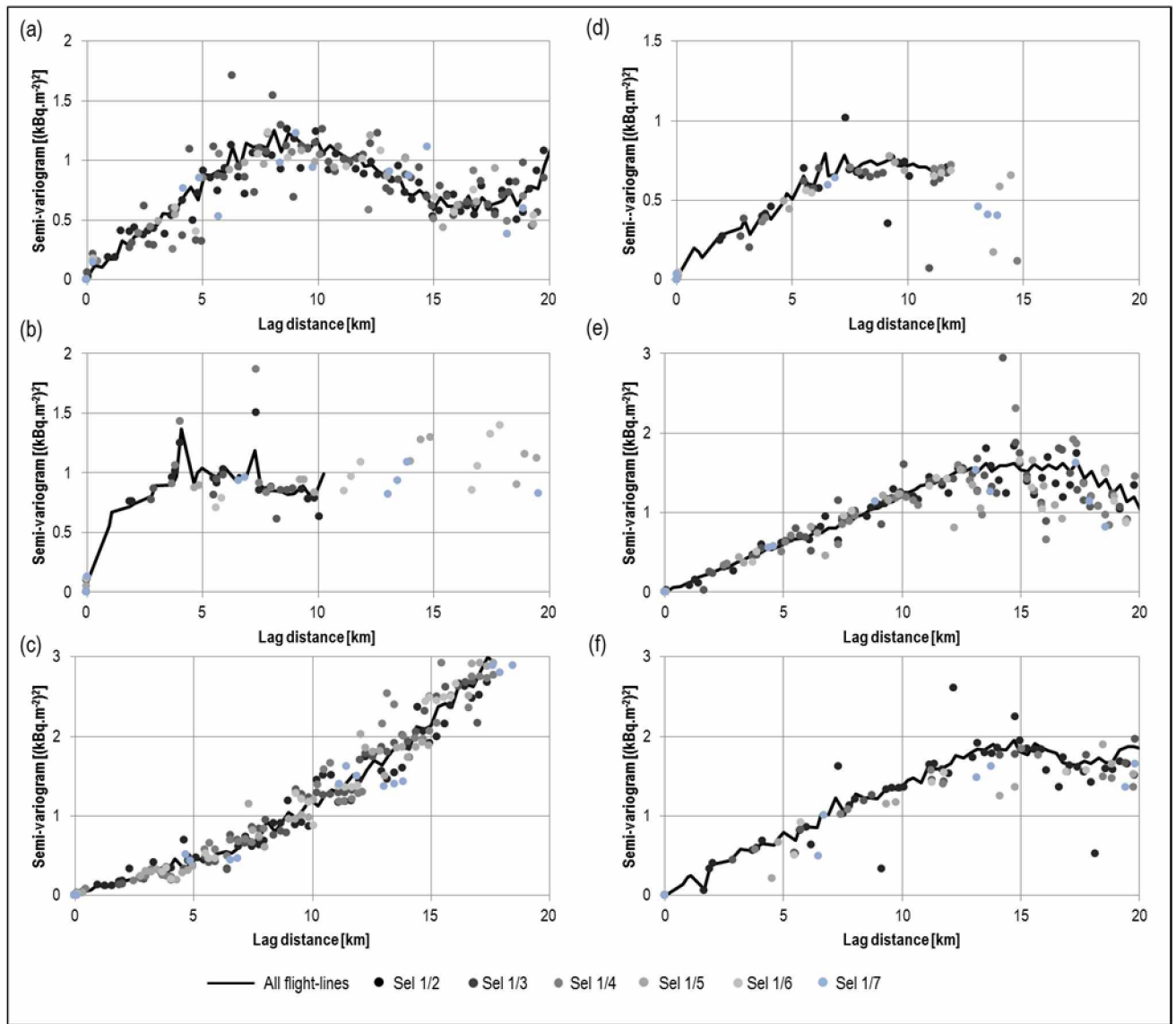
364

365 Fig. 2. Distribution of SRTM DEM elevation (Rabus et al., 2003) (a), land cover types (JAXA , 2018) (b)  
 366 and <sup>137</sup>Cs ground deposit from airborne #8 dataset (c) for test sites T1 to T6.



367

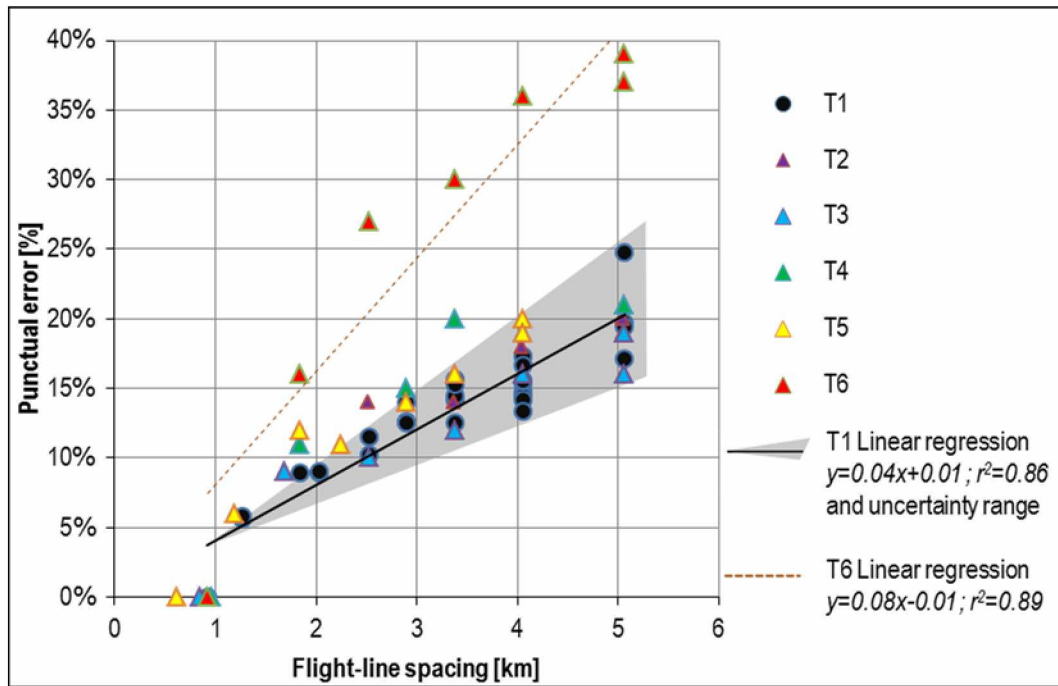
368 Fig. 3. Schematic partitioning of whole the study area according to the “considered as” real and  
 369 characterized contaminated areas: S0 and S1 are correctly characterized surfaces while S2 and S3 are  
 370 false negative and false positive characterized surfaces, respectively.



371

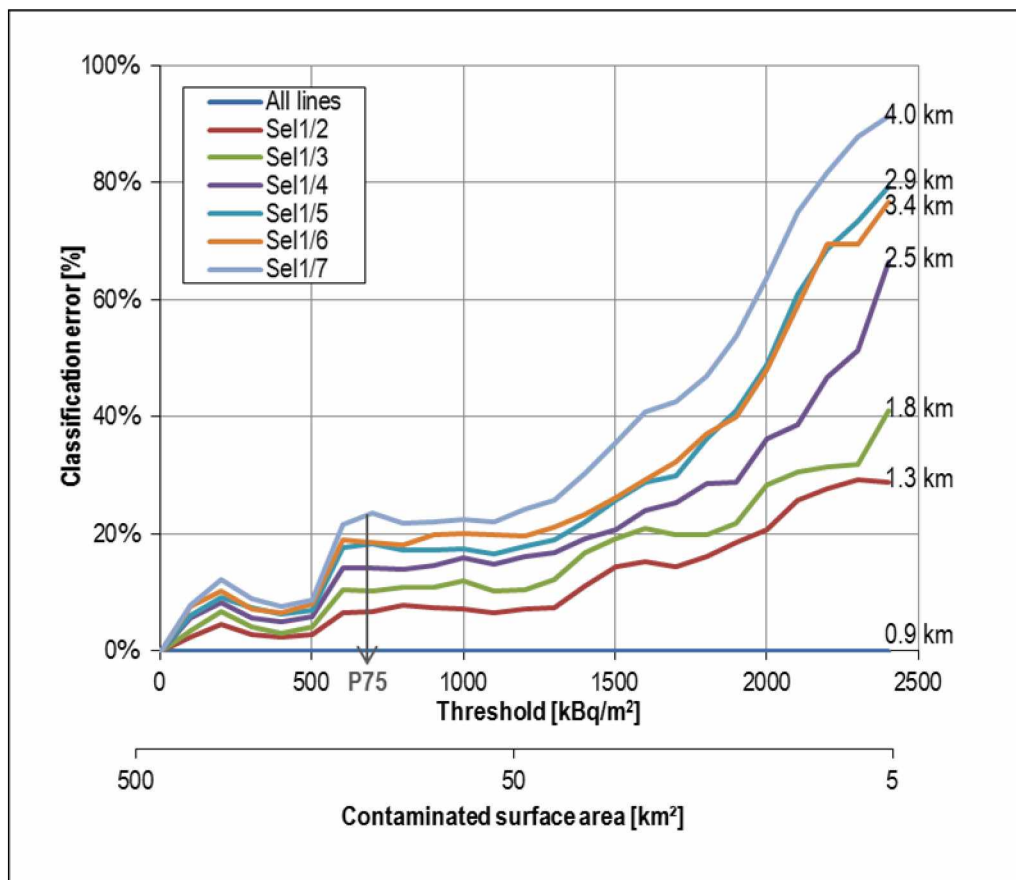
372 Fig. 4. Experimental semi-variogram computed orthogonal to the flight-lines for test sites T1 to T6 (a  
 373 to f) with various flight-line selections.

374



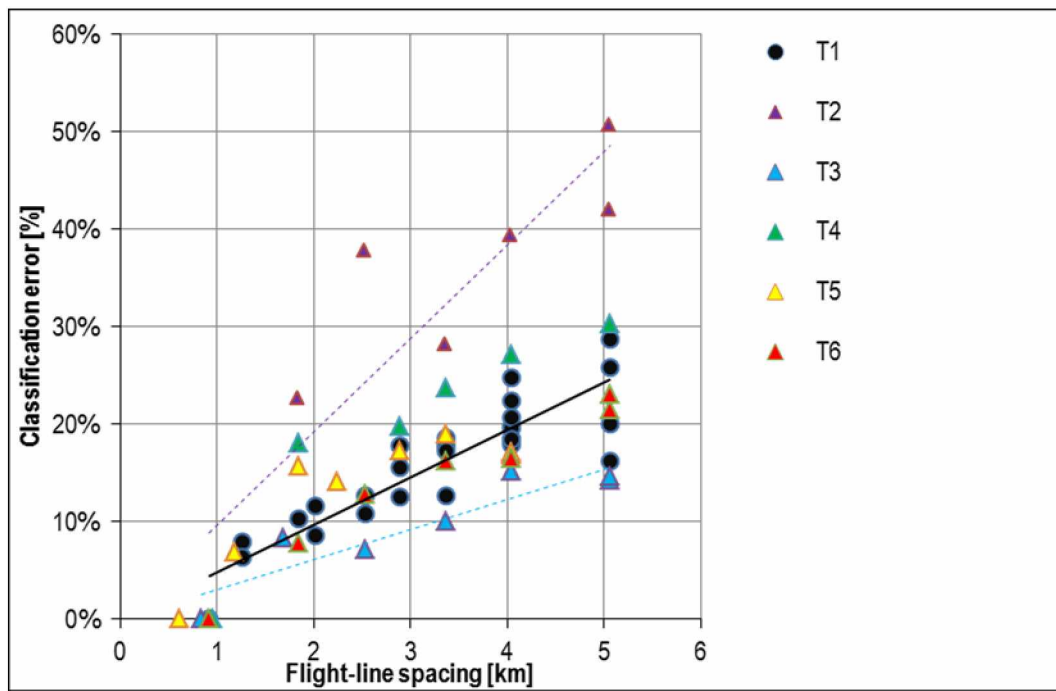
375

376 Fig. 5. The punctual error of validation data versus flight-line spacing, following applying point  
 377 ordinary kriging.



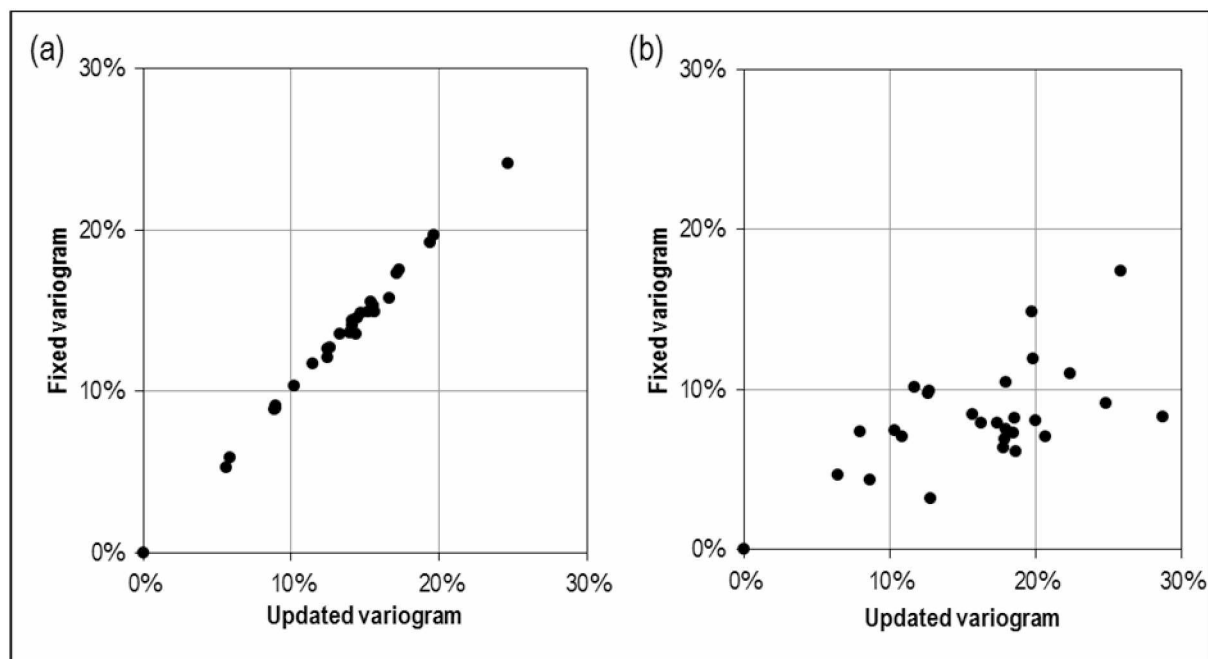
378

379 Fig. 6. The classification error versus threshold and corresponding contaminated surface area, test  
380 site T1.



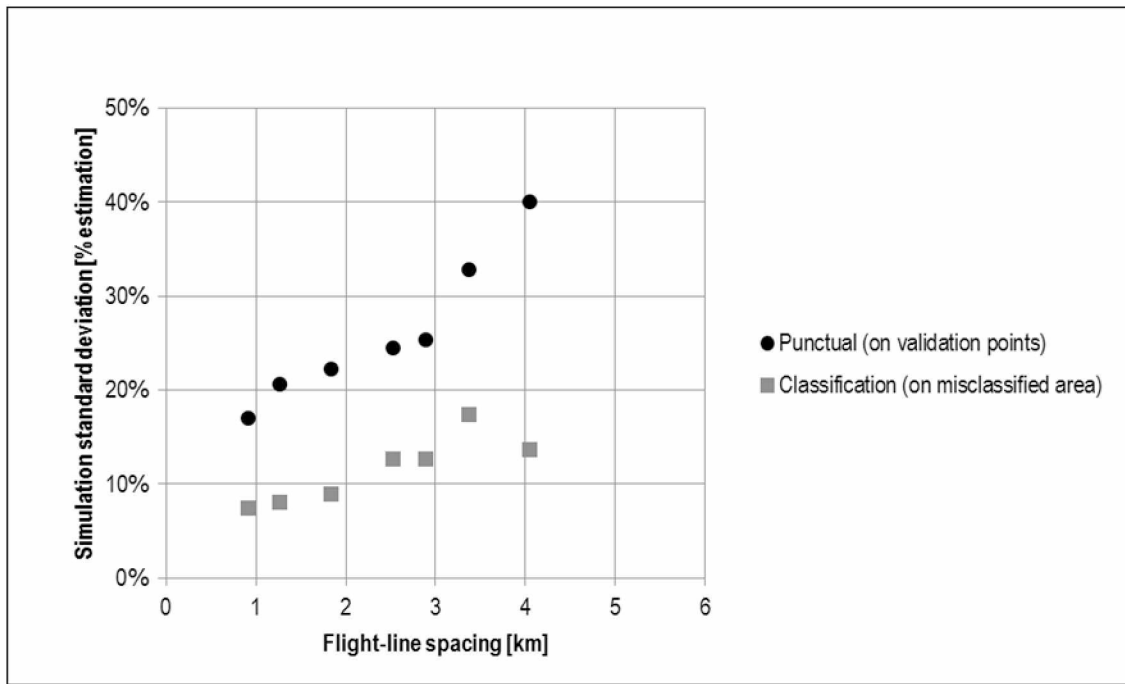
381

382 Fig. 7. The classification error versus flight-line spacing, following applying block ordinary kriging. The  
383 threshold is always P75 (Table 2).



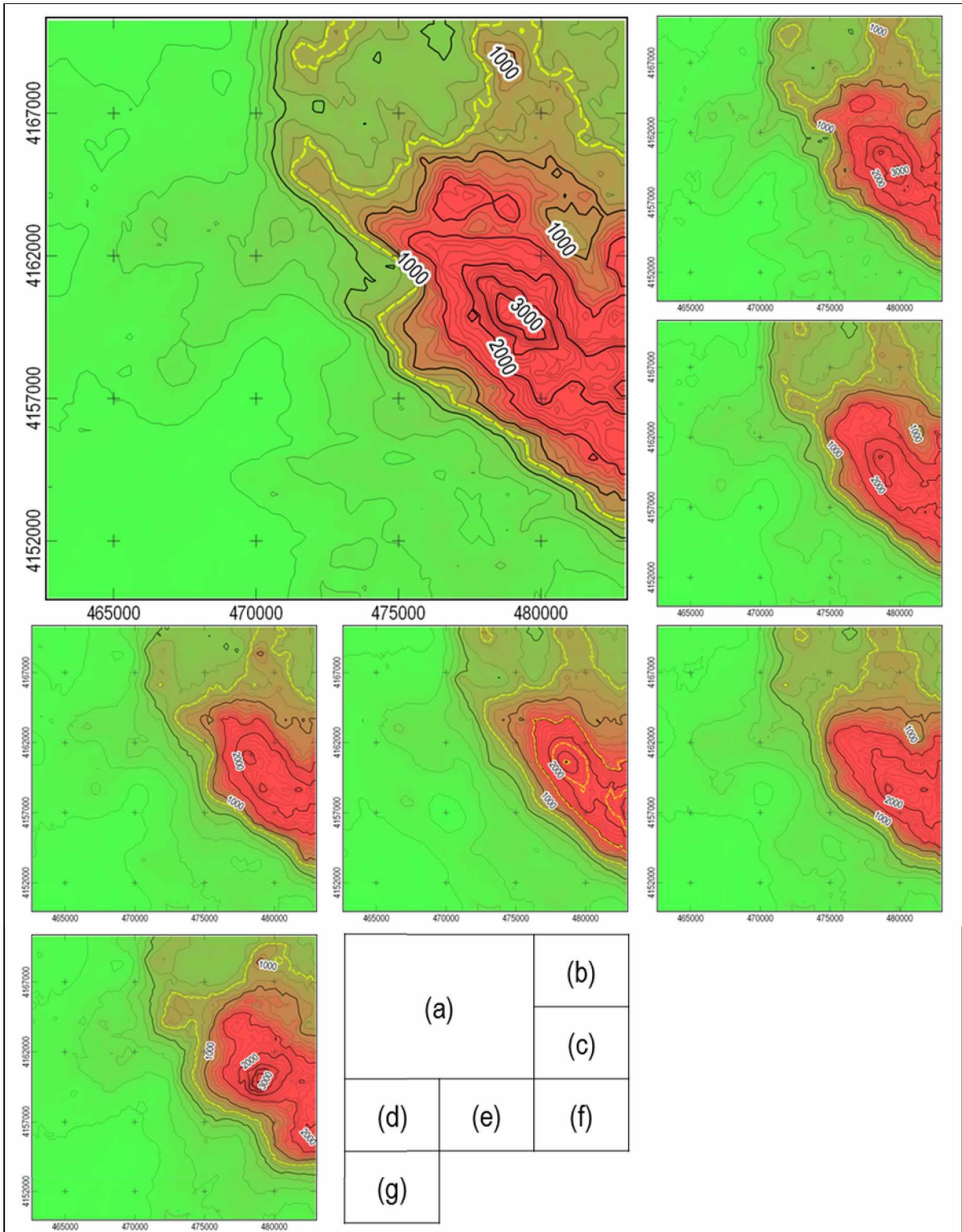
384

385 Fig. 8. Sensitivity of punctual (a) and classification (b) errors according to subjective variography  
386 analysis, in test site T1.



387

388 Fig. 9. Standard deviations of the  $^{137}\text{Cs}$  values simulated at validation points and of the simulated  
389 misclassified areas for test site T1.



390

391 Fig. 10. Contamination map of  $^{137}\text{Cs}$ , estimated by block kriging at the grids of  $250\text{ m} \times 250\text{ m}$  in test  
 392 site T1, using all flight-lines (a), selection 1/2-1 (b), selection 1/3-1 (c), selection 1/4-1 (d), selection  
 393 1/5-1 (e), selection 1/6-1 (f) and selection 1/7-1 (g). The contour values are in  $[\text{kBq}/\text{m}^2]$ . Dashed-line  
 394 is contamination threshold, i.e.  $732\text{ kBq}\cdot\text{m}^{-2}$  (Table 2).